The development of nickel-tungsten carbide functionally graded materials by a laser-based direct metal deposition process for industrial slurry erosion applications

E Yarrapareddy, S Zekovic, S Hamid and R Kovacevic

Proceedings of the Institution of Mechanical Engineers, Part B: Journal of Engineering Manufacture 2006 220: 1923
DOI: 10.1243/09544054JEM578

The development of nickel–tungsten carbide functionally graded materials by a laser-based direct metal deposition process for industrial slurry erosion applications

E Yarrapareddy[1], S Zekovic[1], S Hamid[2], and **R Kovacevic[1]***
[1] Department of Mechanical Engineering, Research Centre for Advanced Manufacturing, Southern Methodist University, Richardson, Texas, USA
[2] Halliburton Energy Services Inc., Carrollton, Texas, USA

The manuscript was received on 24 February 2006 and was accepted after revision for publication on 16 August 2006.

DOI: 10.1243/09544054JEM578

Abstract: Functionally graded materials (FGMs) consisting of Ni–tung (nickel–tungsten carbide) powders with different concentrations of tungsten carbide particles are successfully deposited by a laser-based direct metal deposition (LBDMD) process on 4140 steel substrates. The slurry erosion behaviour of the Ni–tung FGMs is studied at different impingement angles. The slurry erosion tests are performed at Southern Methodist University's Center for Laser-Aided Manufacturing using a centrifugal-force-driven erosion-testing machine. For the purpose of comparison, Ni–tung 40 depositions and 4140 steel samples are also tested. The results indicate that the LBDMD process is able to deposit defect-free Ni–tung FGMs with uniform distribution of tungsten carbide particles in a nickel-based matrix. The slurry erosion resistance of Ni–tung FGMs as observed to be much better than that of the Ni–tung 40 and 4140 steels. The superior slurry erosion resistance of Ni–tung FGMs is attributed to the presence of large amounts of very hard tungsten carbide particles. The material removal rate (MRR) values by erosion decrease with a decrease in the impingement angle, except at a 45° impingement angle on 4140 steel. The relationship among the MRRs, the craters' depth of penetration, the areas of the craters formed, the average surface roughness values, and the impingement angles are established for Ni–tung FGMs, Ni–tung 40, and 4140 steels. The surface profiles of the eroded samples are analysed by measuring the depth of penetration of the craters formed by the slurry jet using a needle-shaped probe and a linear scale with a digital readout. The damaged surfaces are characterized by scanning electron microscopy to investigate the possible application of a material failure model, called damage initiation and damage propagation, to the case of the impingement of a mixture of solid and liquid particles on the Ni–tung FGMs, Ni–tung 40, and 4140 steels. The potentiodynamic polarization curves are generated for the three tested materials and to discover the susceptibility of the material in an erosive environment.

Keywords: functionally graded materials, laser-based direct metal deposition, slurry erosion, characterization, damage initiation and propagation

1 INTRODUCTION

Materials systems developed for slurry erosion resistance provide great benefits in many industries and can improve the service life of systems and components that are exposed to a slurry erosion medium. These materials systems offer excellent resistance to erosion in general, but can be susceptible to damage when a slurry jet impacts the systems. Often the damage in the erosion process resulting from the impact is highly visible and exists in the form of crater profiles and material removal in the system. However, the damage in the erosion process is affected by many process parameters such as the impingement jet velocity, particle size and shape,

**Corresponding author: Department of Mechanical Engineering, Research Centre for Advanced Manufacturing, Southern Methodist University, 1500 International Parkway, Suite no. 100, Richardson, TX, 75081, USA. email: kovacevi@engr.smu.edu*

mechanical and microstructural properties of the target and the solid particles, and angle of impingement.

The functionally graded materials (FGMs) system is designed to achieve better performance than monolithic materials. The performance of FGMs is achieved by the combination of different constituent phase properties. In general, the constituent phases consist of ceramics and metals chosen to decrease the thermal and residual stresses. The ceramic constituent phase provides the heat and corrosion resistance while the metal constituent phase provides the mechanical strength for industrial applications. Hence, the gradient microstructure and property behaviour of FGMs can be tailored for use in different industries for applications such as structural, biomedical, surface erosion resistance, nano-FGMs, and electronics.

There has been a wide variety of processes reported in the literature for FGMs manufacturing. An overview of these manufacturing processes can be found in references [**1**] and [**2**]. FGMs can be produced by powder metallurgy [**3**], shape deposition manufacturing (SDM) [**4**], Laser Engineered Net Shaping (LENS™) [**5**], laser powder deposition (LPD) [**6**], MultiFab [**7**], selective laser sintering (SLS) [**8**], and thermal and/or plasma spraying [**9**] processes. Gradient materials can also be manufactured by electrophoretic deposition [**10**], electrochemical gradation [**11**], and high-energy electron beam irradiation [**12**] processes. Of all these manufacturing processes, the powder metallurgy process is the most commonly used method owing to the controllability of the composition, the microstructure, and the material properties [**13**]. However, owing to several limitations of the powder metallurgy process, the industry is increasingly using the direct metal deposition processes [**4–7**], as a result of their continued development.

In general, slurry erosion is the progressive damage created on solid surfaces by the impact of solid particles carried by a liquid stream. Many segments of industry can benefit from the availability of better slurry erosion resistant materials. Such materials would have significant applications in the oil industry for the drilling and pumping of crude oil from the bottom of the sea or ocean, in mineral industries, and in marine and power production industries. There have been many investigations reported [**14–19**] in the literature regarding the slurry erosion behaviour of monolithic materials. However, there are few studies [**20–22**] reported for the slurry erosion resistance of FGMs. Hence, the focus of this research is the development of Ni–tung FGMs for industrial slurry erosion applications.

The purpose of the present work is the development of the best erosion resistance materials system for industrial applications. Initial studies [**23**] started with the monolithic depositions of Ni–tung 60, A11–LVC tool steel and Inconel 625 powders on 4140 steel substrates, and found the degree of resistance of these materials to erosion. From these results, it was concluded that the Ni–tung 60 performs well for slurry erosion resistance. The work has been extended to research the development of Ni–tung FGMs using the laser-based direct metal deposition (LBDMD) process for industrial slurry erosion resistance applications. The deposited Ni–tung FGMs have been tested for slurry erosion at different impingement angles. The slurry erosion resistance was correlated with the microstructures, the characteristic profiles of the craters formed, and the polarization curves. Furthermore, the slurry erosion resistance of Ni–tung FGMs has been compared with that of monolithic Ni–tung 40 depositions and 4140 steel sample results.

2 EXPERIMENTAL PROCEDURES

2.1 Materials details

The metallic premixed powders used for the development of FGMs are Ni–tung 40, Ni–tung 50 and Ni–tung 60. Ni–tung powders consist of a high percentage of discrete tungsten carbide particles in a nickel-based matrix. The chemical compositions of these powders are shown in Table 1. All of these powders are in the mesh size of $-140 + 325$. The apparent density and Rockwell hardness value of Ni–tung 60 powder is $7.8\,g/cm^3$ and $50\,g/cm^3$, respectively. The morphologies of Ni–tung 40 and Ni–tung 60 powders are shown in Figs 1(a) and (b). These powders consist of angular pieces of tungsten carbide and a mixture of spheroidal and nodular particles that make up the binding material. The absence of the flake-shaped particles of the binding material can partially explain why this powder works well for laser deposition applications. The processes of laser cladding and laser deposition generally work well with spheroidal particles, while the success of these processes with flakey particles is far more limited owing to the high surface area to volume ratio of flake-shaped particles. Thin flat particles tend to superheat when exposed to the laser heat source, resulting in poor depositions. An AISI 4140 steel plate with the approximate dimensions of $30.4\,mm \times 25.4\,mm \times 6.4\,mm$ is used as a substrate

Table 1 The chemical composition of Ni–tung 40, 50, and 60

Element	C	Si	P	S	Cr	Mo	Co	Fe	B	W	Ni
Ni–tung 40	2.90	1.39	0.006	0.001	0.24	0.03	0.02	0.1	0.58	37.1	Bal.
Ni–tung 50	2.75	1.39	0.006	0.001	0.24	0.03	0.02	0.1	0.58	47.25	Bal.
Ni–tung 60	2.80	1.39	0.006	0.001	0.24	0.03	0.02	0.1	0.58	57.22	Bal.

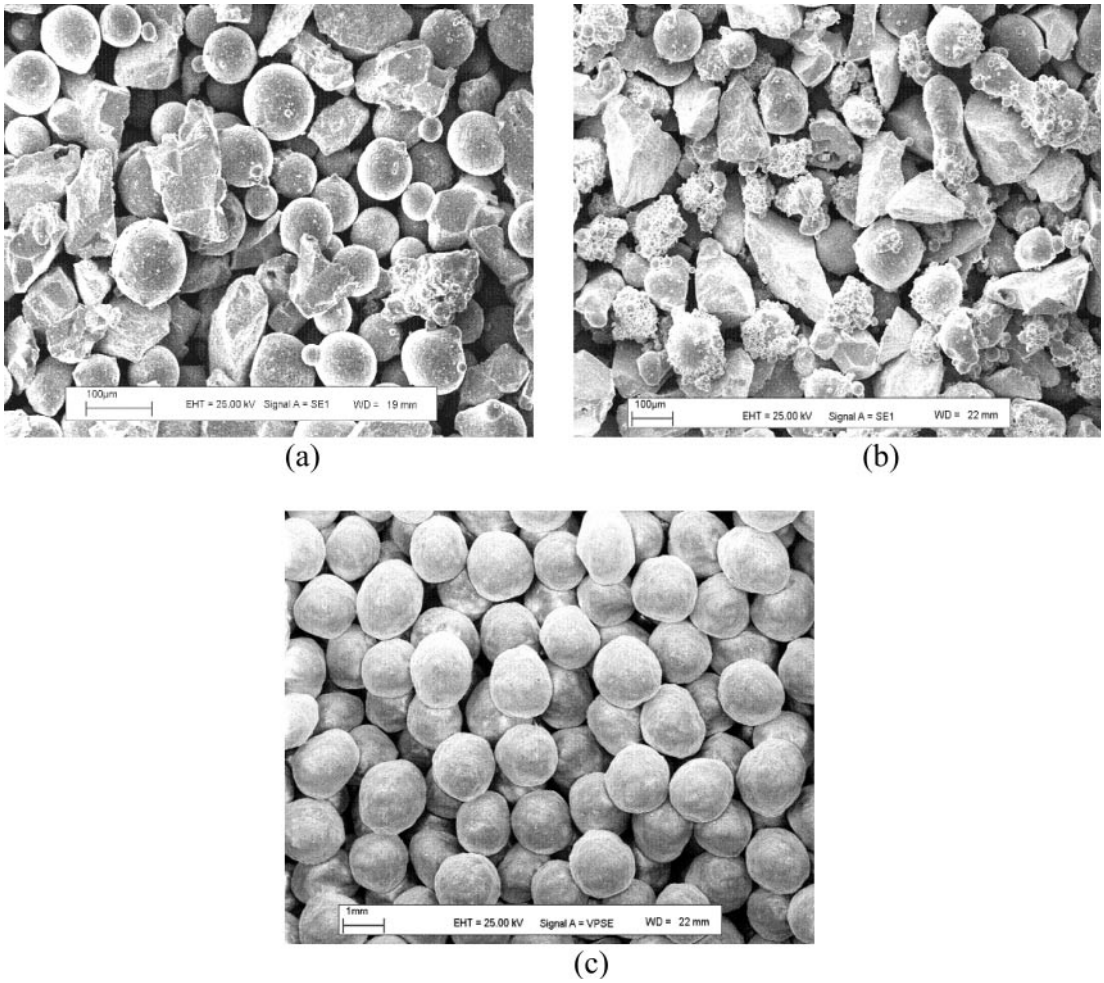

Fig. 1 The morphology of (a) Ni–tung 40; (b) Ni–tung 60 powders; and (c) Econoprop 20/40. Note the difference in magnification among the micrographs

for all depositions. The chemical composition of AISI 4140 steel is 0.38–0.43 C, 0.75–1.00 Mn, 0.15–0.35 Mo, 0.8–1.10 Cr, max. 0.035 P, max. 0.04 Si, and the balance is Fe. A semi-crystalline alumina silicate called Econoprop 20/40 of mesh size $-20 + 30$ is used as a ceramic proppant for slurry erosion testing. The nominal chemical composition of this proppant is shown in Table 2 and the morphology is shown in Fig. 1(c). The Econoprop consists of spheroidal mineral particles with a uniform shape and a narrow size distribution.

Table 2 The chemical composition of Econoprop 20/40

Ingredients	Percentage concentration
Silicon dioxide amorphous	5–35
Mullite crystalline	60–85
Silica crystalline	0–20

2.2 MultiFab system at Southern Methodist University

The Center for Laser-Aided Manufacturing (previously part of the Research Center for Advanced Manufacturing, RCAM) at Southern Methodist University is developing a multi-functional hybrid fabrication system for rapid manufacturing (RM) and repair called Multi Fabrication (MultiFab) [**7**]. The MultiFab is based on additive and subtractive procedures and is able to build the materials directly from the alloy powders using the laser or microplasma as a heat source.

The MultiFab system consists of a five-axis, vertical computer numerically controlled (CNC) milling machine for positioning, milling, drilling, and taping operations, with a 16-tool tool exchanger, a six-axis robot to manipulate and control the microplasma welding torch, and a multimode laser beam for laser metal deposition generated by a Nd:YAG laser of 1 kW in power in a continuous wave (CW) mode and 2.5 kW in a modulated mode. The laser beam is delivered to the laser head through a 1000 μm step index fibre optic cable. The laser head is mounted on the six-axis robot and is cooled by water. The laser head is equipped with four radially symmetric nozzles set at 30° with respect to a vertical axis.

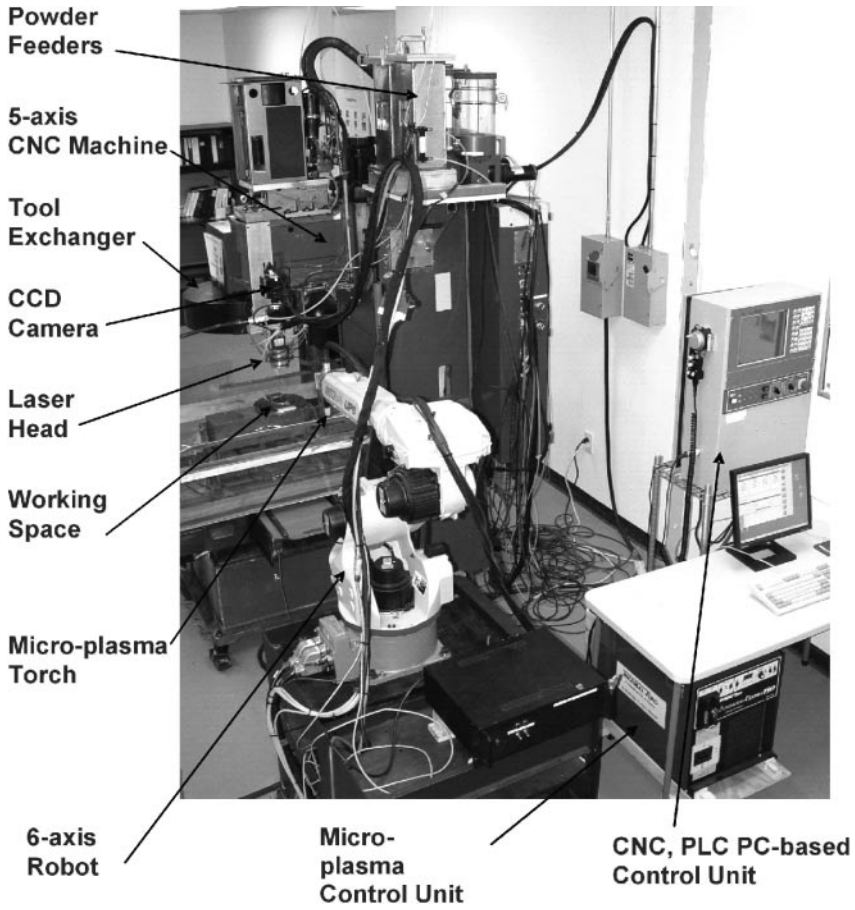

Fig. 2 The MultiFab system at the Center for Laser Aided Manufacturing of Southern Methodist University

These nozzles deliver powder carried by inert gas (argon) to the laser focal point (or molten pool). Two servo-motor driven powder feeders provide stable powder flow for powder delivery. The control system of the laser deposition process is based on a high-frame-rate charge-coupled device (CCD) camera equipped with an infrared (IR) filter to capture the shape of the molten pool in real time, and a laser diode is used for the build-up height measurement. Both the camera and diode laser are installed on the laser head. The CCD camera is coaxial with respect to the laser beam. The MultiFab system is shown in Fig. 2. The MultiFab system can be used for the LBDMD process as well as for the micro-plasma deposition (MPD) process.

2.3 Ni–tung FGMs and Ni–tung 40 deposition profiles and process parameters

The Ni–tung FGMs and Ni–tung 40 are deposited on 4140 steel substrate plates. Four layers of different Ni–tung compositions are deposited on the substrate to build the Ni–tung FGM sample of an approximate size of 30 mm × 25 mm × 1.72 mm. The deposition profile used for Ni–tung FGMs is one layer of Ni–tung 40, one layer of Ni–tung 50, and two layers of Ni–tung 60. These layers are deposited one over the other as shown in Fig. 3(a). Here, Ni–tung 40 and 50 layers act as intermediate layers or supporting layers for the Ni–tung 60, which acts as the working layer. Hence, the Ni–tung FGMs with graded composition from the bottom layer to the top layer are designed to reduce the thermal expansion mismatch among the different deposition layers and the substrate [**20**, **24**, **25**]. Also, here the tungsten carbide ceramic phase provides the heat and erosion resistance, while the nickel matrix provides the mechanical strength. For the purpose of comparison, two layers of Ni–tung 40 are deposited on the substrate with an approximate size of 30 mm × 25 mm × 0.86 mm. These layers are deposited one over the other as shown in Fig. 3(b). The Ni–tung FGMs and Ni–tung 40 depositions are fabricated with a laser beam power of 350–380 W and a 1 mm diameter laser spot. Higher laser power is used for the first layer and lower values are used for the second and successive layers. The linear traverse speed used is 8–10 mm/s and the powder delivery speed is 8–10 g/min with argon as a powder carrier. Each layer is 0.43 mm high and 1 mm wide. A 40 per cent overlap

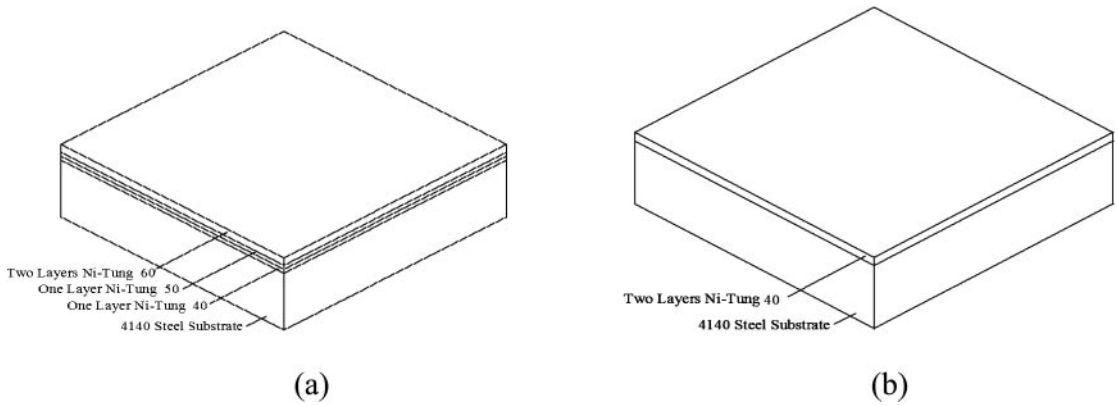

Fig. 3 The schematic representation of deposition profiles used for building (a) Ni–tung FGMs and (b) Ni–tung 40 depositions

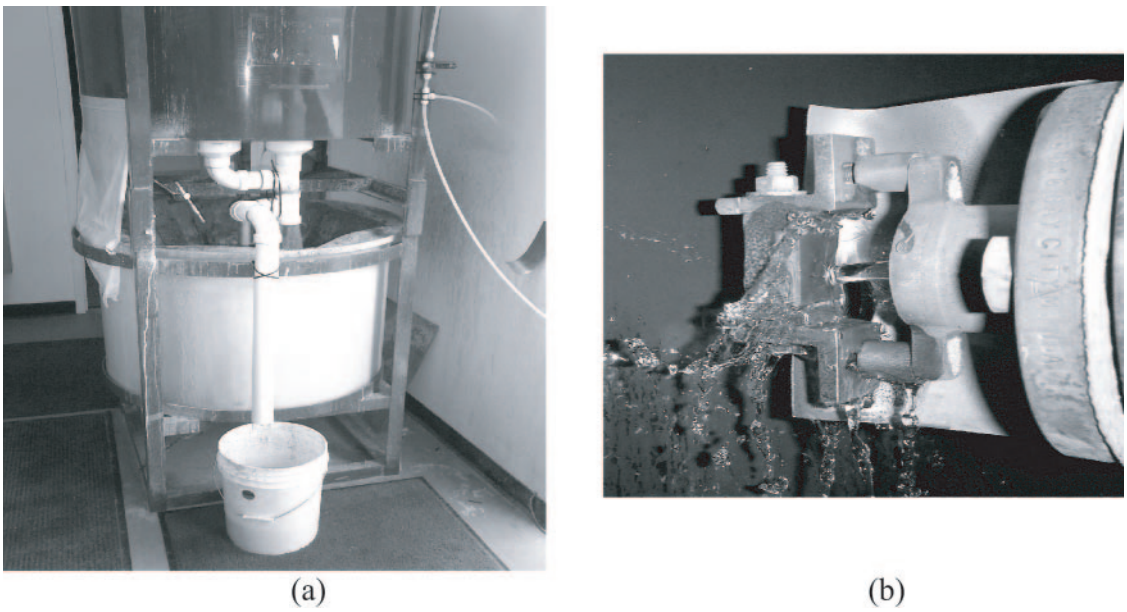

Fig. 4 The slurry erosion testing set up: (a) showing the upper and lower tanks; and (b) showing the slurry jet impinging the test sample at a 90° angle

of successive melting layers is used for all depositions for a uniform surface of the built-up layer.

2.4 The slurry erosion machine, samples testing conditions, and parameters

The slurry erosion tests are conducted at room temperature using the slurry erosion testing machine shown in Fig. 4(a), which consists of two tanks, vertically arranged, with a motor-driven axle running through the upper tank and down into the lower tank. The rotation of the axle provides a centrifugal force that drives the circulation of fluid through the test machine. The upper tank encloses a pair of jet orifice assemblies that hold the test samples at a fixed position relative to the slurry jet, and rotate at the ends of the two hollow arms that are attached to the axle. The orifices are each 6.4 mm in diameter. Fluid that flows out of the orifices during testing first strikes the samples as shown in Fig. 4(b), then falls to the bottom of the upper tank where it is funnelled through a single large orifice to fall to the lower tank. The lower tank serves as a fluid reservoir for the test machine. A mixing element at the bottom of the axle stirs the fluid in the lower tank and provides a near-homogeneous mixture of liquid and solid components. Here the liquid component used is water and the solid component used is Econoprop 20/40.

For all experiments, the slurry concentration used is 22.73 kg (50 pb) of Econoprop 20/40 in 94.64 l (25 gal) of water. This concentration is maintained constant at all testing times. Experiments are carried out at a slurry impingement velocity of 25 m/s and tested at 30°, 45°, and 90° impingement angles. The impingement time used is 10 min per test sample.

The mixing shaft element speed is set at 875 r/min for all experiments. The test samples are cleaned with methyl alcohol before and after testing, and weighed for the mass loss using an electronic scale with an accuracy of 0.1 mg. Two samples are used for each impingement angle; hence, 12 samples are tested altogether. The mass loss per unit quantity of time, called the material removal rate (MRR), is calculated using the following formula.

$$\text{Material removal rate, (MRR)} = (W_\text{i} - W_\text{f})/(\text{unit quantity of time}) \quad (1)$$

Here W_i is the initial mass of each sample and W_f is the final mass after erosion testing.

2.5 Test samples' preparation and characterization

The as-deposited Ni–tung FGMs and Ni–tung 40 samples are surface ground to remove the loose, unmelted powder particles and to remove protruding corner depositions from the surfaces of the deposits. The samples are surface ground until a smooth surface appears. This result is necessary to achieve accurate MRR values. The microstructure of the samples is examined by light optical microscopy (LOM) and scanning electron microscopy (SEM). The samples for LOM analysis are prepared by the standard metallographic procedure. The SEM characterization is used to observe the surfaces and subsurfaces of the eroded samples to evaluate the damage initiation and the successive damage propagation. The elemental composition of deposited surfaces is analysed by the electron probe coupled with energy dispersive spectrometry (EDS) using CuKα radiation at a 2θ angle. The damaged samples' surfaces are also characterized by measuring the maximum penetration depth of the crater formed by the slurry jet using the needle-shaped probe and a linear scale with a digital readout. The average surface roughness values are measured by the portable surface roughness measurement tester. This tester is able to measure roughness between –200 μm and 150 μm. The potentiodynamic polarizations curves are generated at room temperature for the three test samples based on ASTM G61–86 standard test procedure using PowerCORR [**26**] corrosion measurement software.

3 RESULTS AND DISCUSSION

3.1 Morphologies and microstructures of laser deposited Ni–tung FGMs, Ni–tung 40, and 4140 Steels

In order to study the behaviour of slurry erosion resistance of the deposited materials, it is first necessary to characterize their microstructures. The as-deposited Ni–tung FGMs' cross-sectional microstructure from the optical microscopy is shown in Fig. 5. This microstructure has shown the gradient change in the composition of the constituent phases in the vertical direction. The discrete tungsten carbide particles are uniformly distributed in a primary face centred cubic nickel-based matrix in each layer. The tungsten carbide particles provide the solution strengthening to the matrix. The EDS analysis of Ni–tung FGMs revealed that the cross-sectional microstructure of the first layer consists of 40 per cent tungsten carbide phase, the second layer consists of 50 per cent tungsten carbide phase, and next two layers consists of 60 per cent tungsten carbide phase. The dilution between the successive deposited layers is good owing to the higher solidification rates of the LBDMD process. These FGMs layers produced porosity-free and crack-free microstructures. A higher magnification microstructure shown in Fig. 6(a) for the top view of Ni–tung 60 layers reveals the uniform distribution of tungsten carbide particles in a nickel-based matrix. The detailed microstructure of Ni–tung powders processed by hot isostatically pressing (HIP) can be found in the literature [**27**]. In the HIP process, the tungsten carbide particles maintain their position in the matrix during the filling and consolidation [**27**] of the powder metallurgy process as well as in the LBDMD process. The microstructure of the 4140 steel sample is shown in Fig. 6(b); the constituent phases for martensite and bainite are visible.

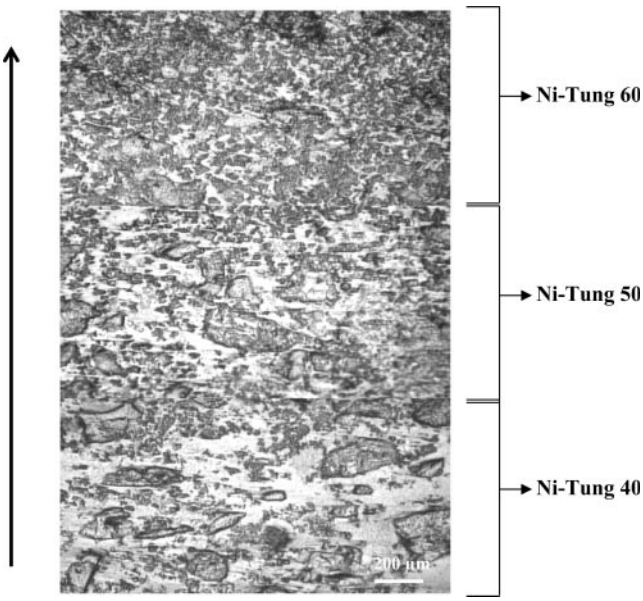

Fig. 5 The cross-sectional view of Ni–tung FGMs showing the different successive layers with gradient microstructure. The vertical arrow shows the deposition direction

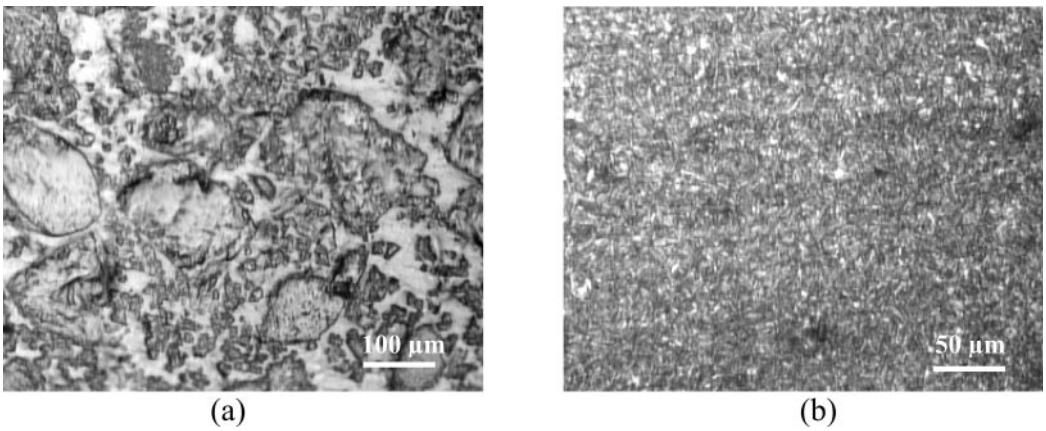

Fig. 6 The optical microstructure of (a) Ni–tung FGMs' top layer (Ni–tung 60) showing the distribution of tungsten carbide particles in the nickel-based matrix and (b) the 4140 steel showing the constituents phases martensite and bainite

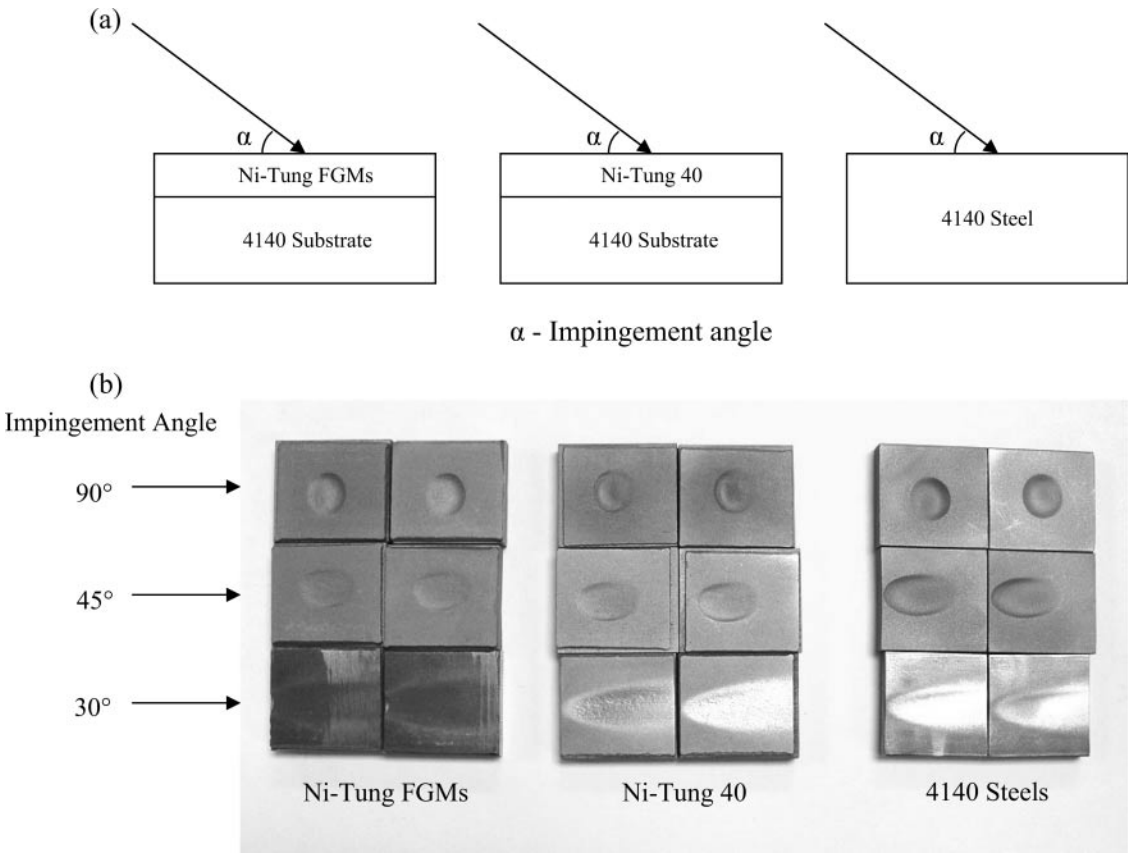

Fig. 7 (a) The schematic representation of slurry jet impingement angle for different materials tested and (b) showing the Ni–tung FGMs, Ni–tung 40, and 4140 steel samples after erosion testing

3.2 MRRs, depth of penetrations, area of craters formed, and surface roughness values

In order to evaluate slurry erosion resistance of Ni–tung FGMs, Ni–tung 40 and 4140 steels are tested for erosion at different impingement angles as shown in Fig. 7(a). The erosion tested samples' macrographs are shown in Fig. 7(b). The graph showing the MRR values at different impingement angles is shown in Fig. 8. The MRR values show that the Ni–tung FGMs and Ni–tung 40 perform better at lower impingement angles than at higher impingement angles. In contrast, the ductile 4140 steel suffers the most severe erosion at an angle of

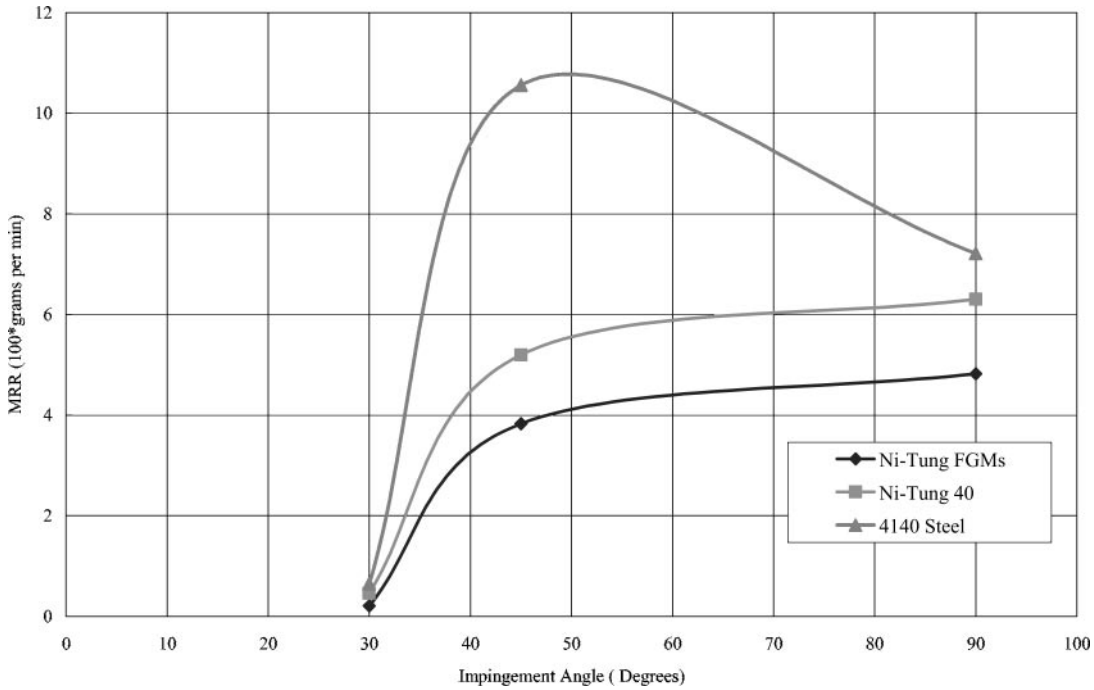

Fig. 8 The graph showing the MRR values at different impingement angles for different tested materials

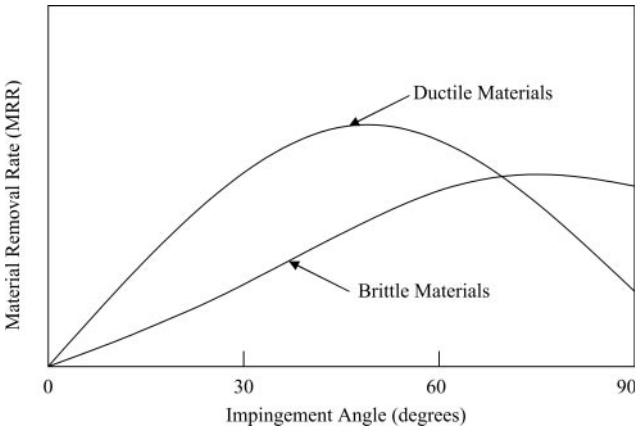

Fig. 9 Schematic representation of MRR on impingement angles for ductile and brittle materials [**30**]

45°. This kind of characteristic feature is well known in dry erosion, where ductile materials usually show greater erosion at low impingement angles with respect to the brittle materials, and vice versa [**28**, **29**]. The schematic representation of ductile and brittle materials' erosion resistance for different impingement angles is shown in Fig. 9 [**30**]. However, it is reported that such trends are less clear in the slurry erosion [**28**]. The excellent erosion resistance of Ni–tung FGMs at all impingement angles is attributed to the amount of hard phase tungsten carbide particles.

The maximum penetration depths of the slurry erosion patterns formed at different impingement angles is shown in Fig. 10. For a 90° impingement angle, the penetration depth for Ni–tung FGMs is 0.95 mm, for Ni–tung 40 it is 1.34 mm, and for 4140 steels it is 1.69 mm. The materials are severely damaged at that angle. However, for 4140 steel, the most severe damage with respect to the other two materials occurred at a 45° impingement angle with a penetration depth of 1.58 mm. At a 30° impingement angle, all three materials performed well for slurry erosion resistance. The penetration depths recorded are very low: 0.03 mm, 0.07 mm, and 0.09 mm are recorded for Ni–tung FGMs, Ni–tung 40, and 4140 steels, respectively.

The areas of the craters formed (*X*–*Y* plane) are measured using the linear scale with a digital readout. The areas of the craters formed at different impingement angles are shown graphically in Fig. 11. The areas of the craters formed for Ni–tung FGMs, Ni–tung 40, and 4140 steels at 90° and 30° impingement angles are 71.33, 78.67, and 104.07 mm^2 and 218.36, 283.70, and 306.02 mm^2, respectively. From these values, it can be illustrated that the areas of craters formed increase with a decrease of the impingement angles. This area increase is inevitable owing to the large area of travel of the slurry jet at lower impingement angles; hence, at lower impingement angles, the MRR values decrease.

The original average surface roughness (R_a) values for Ni–tung FGMs, Ni–tung 40, and 4140 steel are 0.74 μm, 0.96 μm, and 1.05 μm,

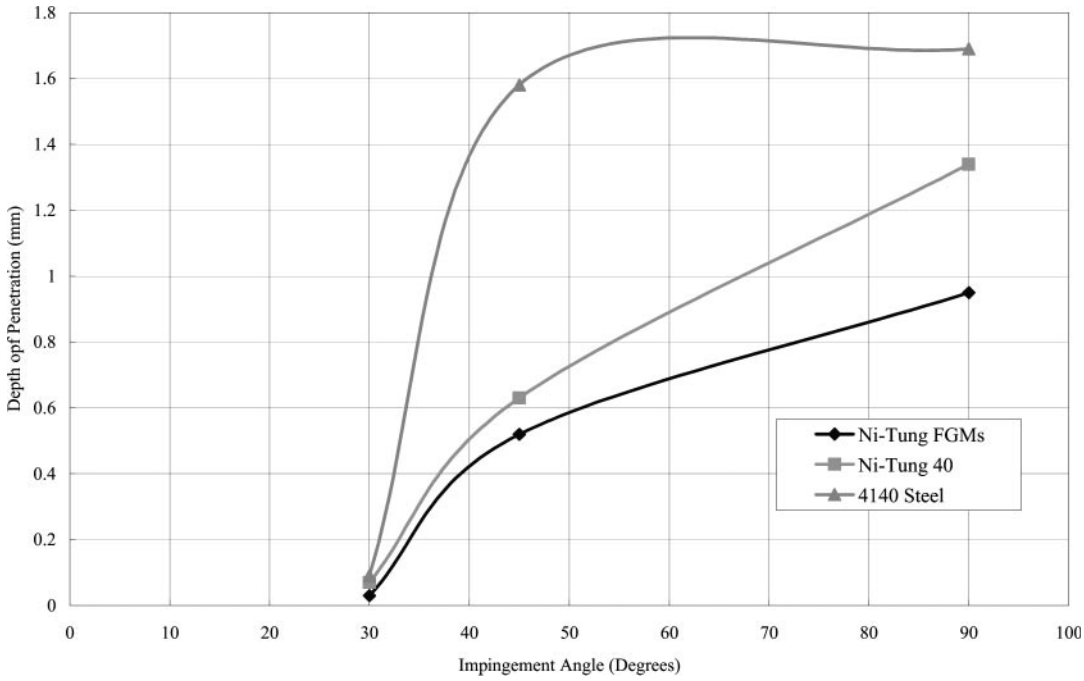

Fig. 10 The graph showing the relationship between the depth of penetration as a function of slurry jet impingement angle

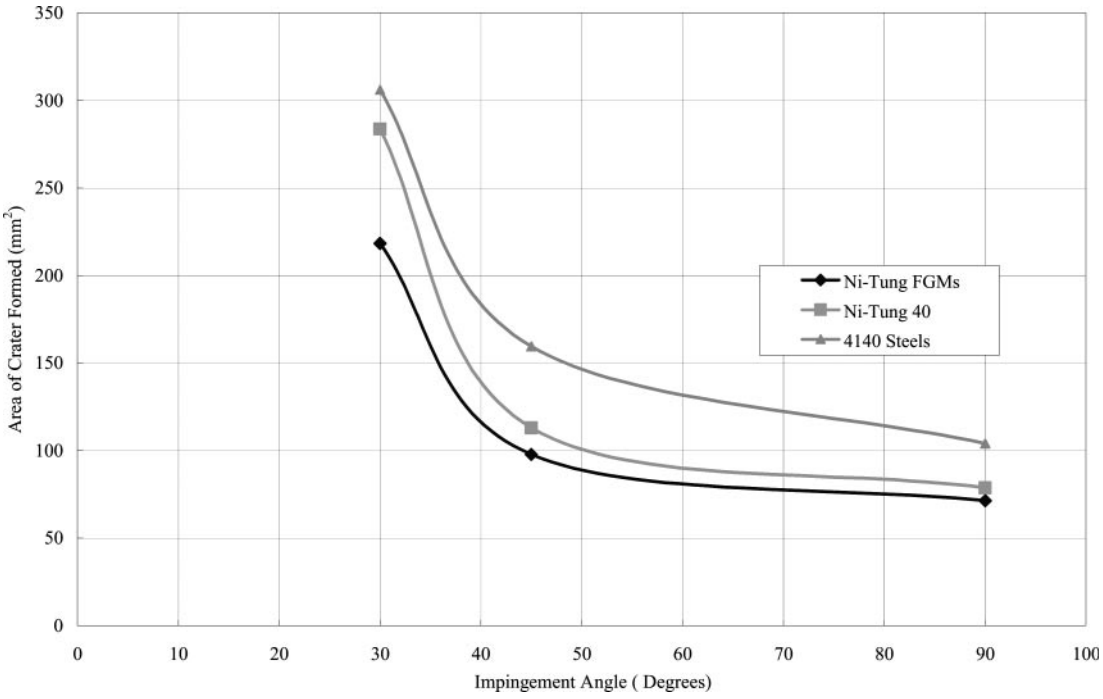

Fig. 11 The graph showing the relationship for the area of craters formed at impingement angles for Ni–tung FGMs, Ni–tung 40, and 4140 steels

respectively. The average surface roughness values increased after slurry erosion testing at different impingement angles as represented in Fig. 12. Also, the average surface roughness values increase with an increase of the jet impingement angles. For a 45° slurry jet impingement on 4140 steel, the average surface roughness value is 3.32 μm. The higher R_a values are attributed to the presence of surface ripples (as shown in Fig. 13) after erosion testing.

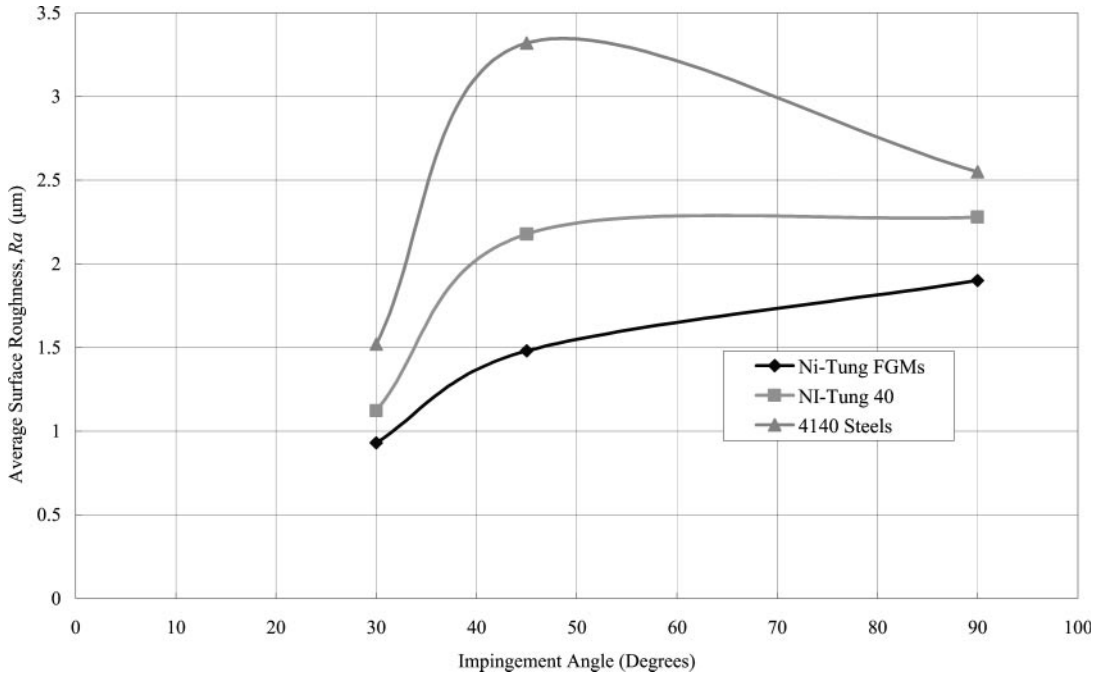

Fig. 12 The graph showing the relationship for the average surface roughness values at different impingement angles for Ni–tung FGMs, Ni–tung 40, and 4140 steels

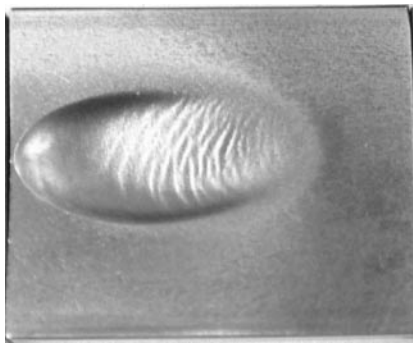

Fig. 13 One of the 45° slurry erosion tested 4140 steel samples showing the presence of surface ripples, which are caused for the higher value of average surface roughness

3.3 SEM characterization of slurry eroded surfaces

The slurry eroded surfaces of the Ni–tung FGMs and Ni–tung 40 are characterized by SEM in order to understand the characteristic features of erosion surfaces, subsurfaces, and the erosion mechanism. Figures 14 and 15 show the typical SEM images of Ni–tung FGMs and Ni–tung 40 damaged surfaces at different impingement angles. The Ni–tung FGMs and Ni–tung 40 are damaged and the material removed when the plastic strain of the material exceeds its failure criteria value when that material is impacted by the high-velocity slurry jet containing both the solid and liquid particles at different impingement angles. Hence, the damage is mainly initiated by the solid (Econoprop 20/40) and liquid (water) particles. This damage is propagated for successive impingements causing micro-cutting and material removal from the surface of the material. Figure 15(a) illustrates the Ni–tung 40 damage from a normal impingement angle and shows the severely damaged surfaces, subsurfaces, and high depth of the field. An increasing number of pits and high degree of micro-cutting of the material are present. Figure 15(c) shows a lower number of pits and fewer micro-cracks on the surface of the sample impinged by a 30° impingement angle of slurry jet. Figure 16 is a high-magnification image for Ni–tung FGMs showing the severe damage of the sample which is impinged by a 90° slurry jet. This image reveals the damage initiation caused by the mixture of solid and liquid particles and this damage is propagated by successive impingements. Finally, the depth of field employed while viewing the samples in the SEM is directly proportional to the jet impingement angle used for a given sample, which supports the earlier penetration depth measurements indicating that larger jet angles create deeper erosion crater zones in the samples.

3.4 Potentiodynamic polarization curves

ASTM G61–86 standard test method [**31**] gives the procedure for conducting cyclic potentiodynamic

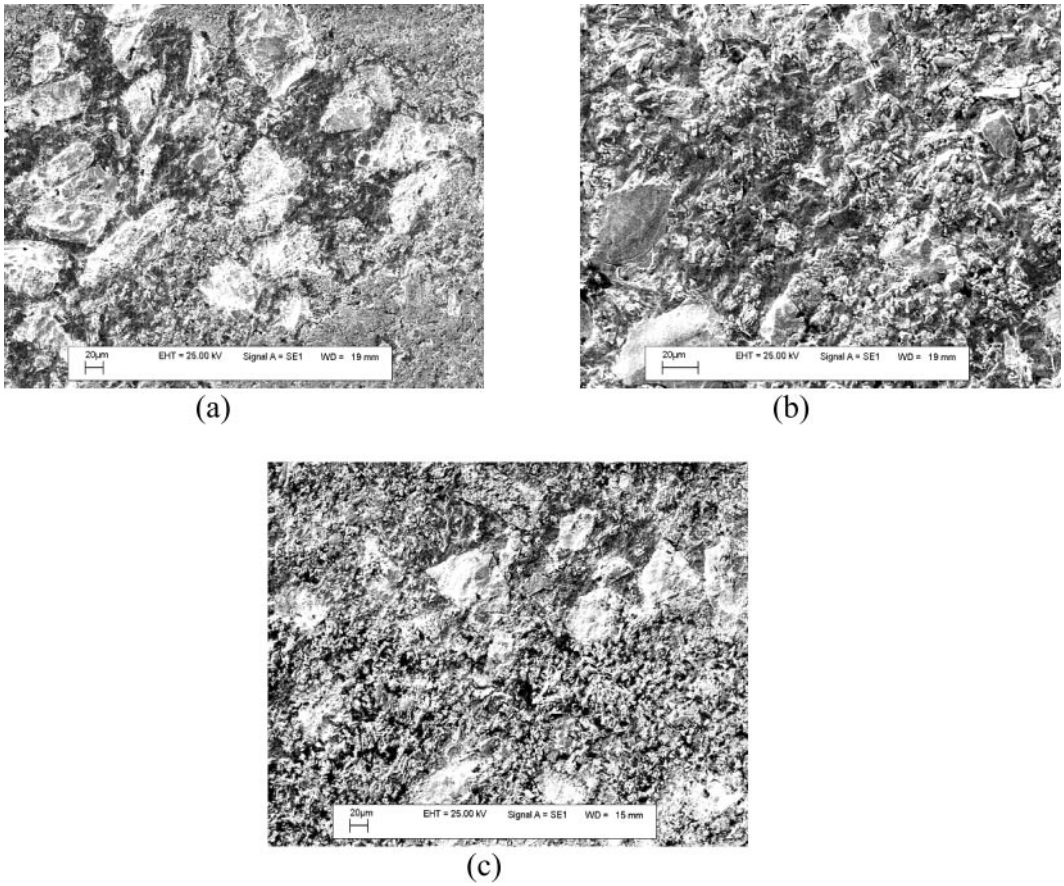

Fig. 14 Typical SEM microstructures of slurry eroded Ni–tung FGMs samples tested at (a) 90°; (b) 45°; and (c) 30° impingement angles. Note the difference in magnification among the micrographs due to difference in depth of penetrations of the craters formed

polarization curves for measuring the relative susceptibility to localized corrosion in an erosive environment. This indication of the susceptibility to the initiation of localized corrosion is determined by the potential at which the anodic current increases rapidly. The more this potential, obtained at a fixed scan rate in this test, the less susceptible the material is to the initiation of localized corrosion. This localized corrosion susceptibility is analogous to the erosion resistance of the material in the given environment [**28**, **32**]. The potentiodynamic polarization curves generated for the Ni–tung FGMs, Ni–tung 40, and 4140 steel samples are shown in Fig. 17. These curves indicate that 4140 steels are electrochemically active, or more susceptible to corrosion, than the Ni–tung FGMs and Ni–tung 40 depositions. Also, the Ni–tung 40 samples are more chemically active towards the erosive environment owing to the presence of a higher amount of nickel-based matrix than in the Ni–tung FGM's top layer with respect to the current density. This result describes how the material behaves when exposed to particular erosive environments and also indicates the ability of the sample to protect itself against an aggressive attack from the erosive environment.

4 CONCLUSIONS

The materials system called the Ni–tung FGMs is able to sustain better slurry erosion resistance than the monolithic materials at different impingement angles. This system was developed and deposited successfully by the LBDMD process with defect-free and crack-free microstructures. This materials system improves the service life of the tools, components, and systems that are exposed to a slurry erosion medium. Also, this materials system was tested for slurry erosion at different impingement angles and characterized by analysing the MRRs, the depth of penetrations, the areas of the craters formed, the average surface roughness values, the microstructures, and the potentiodynamic polarization curves. The slurry erosion resistance of the Ni–tung FGMs is compared with Ni–tung 40 and 4140 steels.

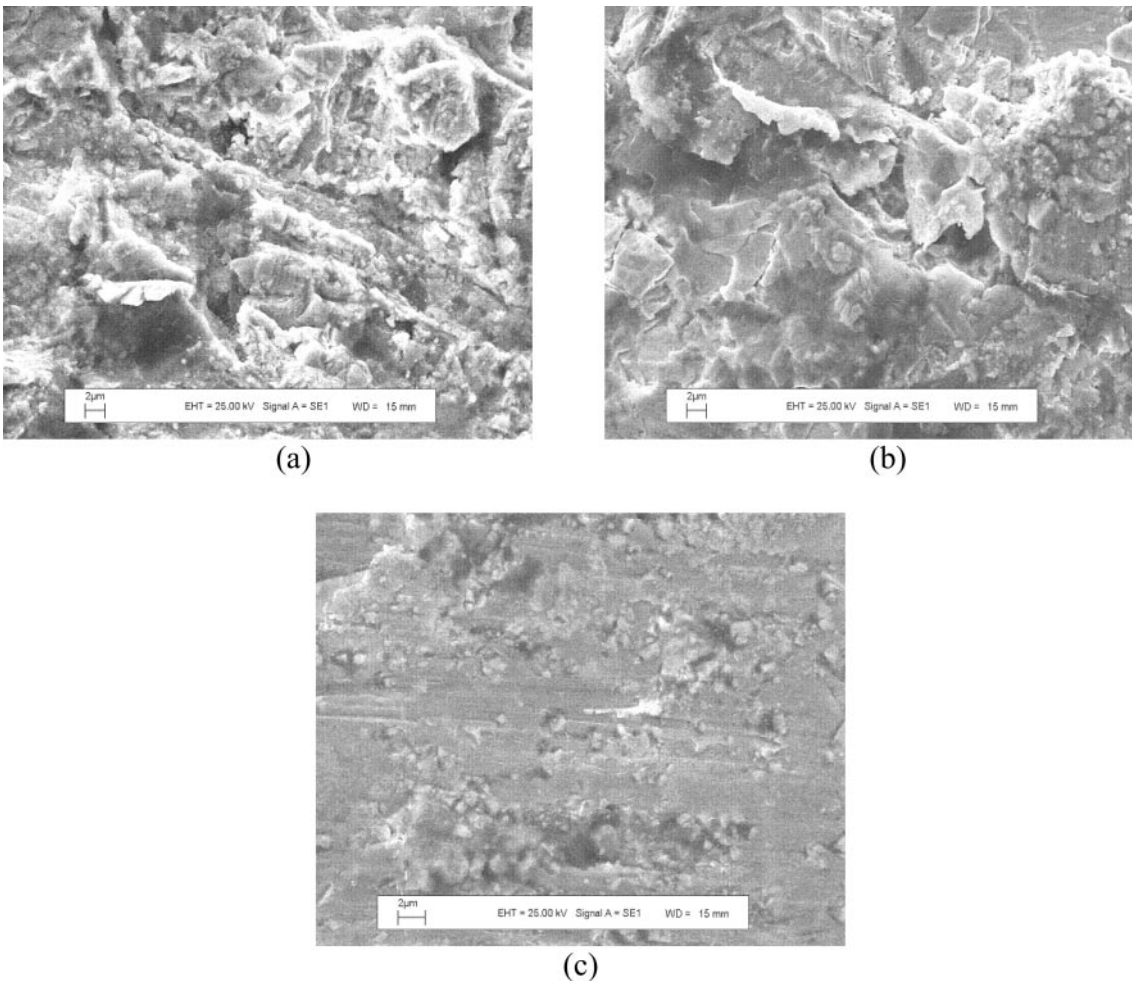

Fig. 15 Typical SEM microstructures of slurry eroded Ni–tung 40 samples tested at (a) 90°; (b) 45°; and (c) 30° impingement angles. Note the difference in magnification among the micrographs due to difference in depth of penetrations of the craters formed

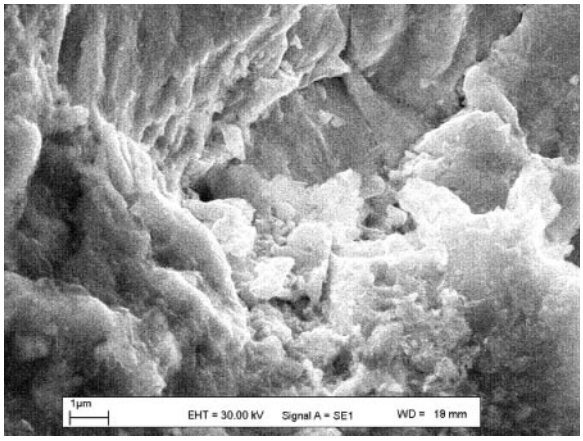

Fig. 16 High magnification SEM image for 90° slurry jet impingement angle for Ni–tung FGMs showing the damage initiation causing the high degree of micro-cutting and material removal, and the damage is propagated for successive impingements

ACKNOWLEDGEMENTS

The authors would like to acknowledge the financial support from Halliburton Energy Services through joining the NSF Industry University Co-operative Research Center for Laser-Aided Manufacturing program (NSF grant no. DMI-0541952). The Ni–tung powders and Econoprop 20/40 were supplied by Carpenter Powder Products and Carbo Ceramics, respectively. The authors would also like to acknowledge Mr Michael Valant for helping to perform the experiments, Dr Haoyue Zhang of Halliburton Energy Services for technical discussions, and Mr Roy Beavers of Southern Methodist University for SEM technical support. Thanks are also extended to Mr Bharat Jasthi, PhD candidate at South Dakota School of Mines and Technology, Rapid City, South Dakota for performing the potentiodynamic polarization tests.

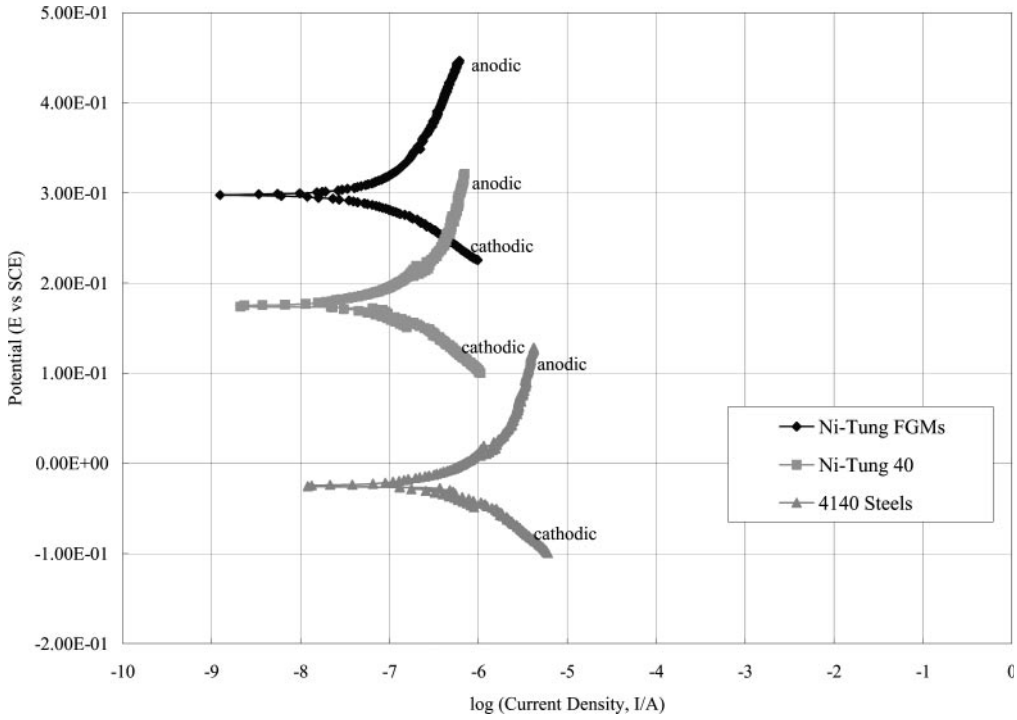

Fig. 17 The potentiodynamic polarization curves generated at room temperature for Ni–tung FGMs, Ni–tung 40 depositions, and 4140 steels

REFERENCES

1 **Mortensen, A.** and **Suresh, S.** Functionally grades metals and metal–ceramic composites: Part 1, Processing. *Int. Mater. Rev.*, 1995, **40**(6), 235–265.

2 **Neubrand, A.** and **Rodel, J.** Gradient materials: an overview of a novel concept. *Z. Metallkd*, 1997, **8**(5), 358–371.

3 **Jin, G., Takeuchi, M., Honda, S., Nishikawa, T.,** and **Awaji, H.** Properties of multilayered mullite/Mo functionally graded materials fabricated by powder metallurgy processing. *Mater. Chemistry and Physics*, 2005, **89**, 238–243.

4 **Fessler, J., Nickel, A., Link, G., Prinz, F.,** and **Fussell, P.** Functional gradient metallic prototypes through shape deposition manufacturing. In Proceedings of the Symposium on *Solid freeform fabrication*, University of Texas at Austin, 1997, pp. 521–528.

5 **Ensz, M., Griffith, M.,** and **Reckaway, D.** Critical issues for functionally graded material deposition by Laser Engineered Net Shaping (LENS™). MPI Fall Conference, 2002, pp. 1–8.

6 *The development of functionally graded materials for manufacturing tools and dies and industrial processing equipment*, DOE Project DE-FC36–04GO14036 (Department of the Environment).

7 **Kovacevic, R.** System and method for fabrication and repairing part. US Pat. 7 020 539 (issued 28 March 2006).

8 **Lepson, L., Beaman, J., Bourell, D.,** and **Wood, K.** SLS processing of functionally gradient materials. In Proceedings of Symposium on *Solid freeform fabrication*, University of Texas at Austin, 1997, pp. 67–79.

9 **Barbezat, G., Nicol, A., Jin, Y., Wang, Y.,** and **Sheng, X.** Abrasive wear performance of Cr_3C_2–25%NiCr coatings by plasma spray and CDS detonation spray. *Wear*, 1995, **38**, 845–850.

10 **Put, S., Vleugels, J., Anne, G.,** and **VanderBiest, O.** Functionally graded ceramic and ceramic–metal composites shaped by electrophoretic deposition. *Colloids and Surf. A*: *Physicochem.*: *Engng Aspects*, 2003, **222**, 223–232.

11 **Jedamzik, R., Neubrand, A.,** and **Rodel, J.** Functionally graded materials by electrochemical processing and infiltration: application to tungsten/copper composites. *J. Mater. Sci.*, 2000, **35**, 477–486.

12 **Oh, S., Suh, D.,** and **Lee, S.** Microstructural of TiN/carbon steel functionally gradient materials processed by high-energy electron beam irradiation. *Mater. Sci. Engng*, 1998, **A248**, 245–255.

13 **Ma, J., Tan, G.,** and **He, Z.** Fabrication and characterization of Ti–TiB_2 functionally graded material system. *Metall. Mater. Trans. A*, 2002, **33A**, 681–694.

14 **Jiang, W.** and **Kovacevic, R.** Slurry erosion resistance of laser clad Fe–Cr–B–Si. *Surf. Engng*, 2004, **20**, 464–468.

15 **Lathabai, S.** and **Pender, D.** Microstructural influence of slurry erosion of ceramics. *Wear*, 1995, **189**, 122–135.

16 **Tan, K., Wood, R.,** and **Stokes, K.** The slurry erosion behavior of high velocity oxy-fuel (HVOF) sprayed aluminum bronze coatings. *Wear*, 2003, **255**, 195–205.

17 **Tucker, T., Clauer, A., Wright, I.,** and **Stropki, J.** Laser-processed composite metal cladding for slurry erosion resistance. *Thin Solid Films – Metall. Protective Coatings*, 1984, **118**, 73–84.

18 **Aso, S., Goto, S., Komatsu, Y., Liu, W.,** and **Liu, C.** Slurry erosion of Fe-15 mass%/25% mass Cr–C–B eutectic alloys. *Wear*, 1999, **233–235**, 166–167.

19 **Dasgupta, R., Prasad, B., Jha, A., Modi, O., Das, S.,** and **Yegneswaran, A.** Slurry erosive wear characteristics of a hard faced steel: effect of experimental parameters. *Wear*, 1997, **213**, 41–46.

20 **Vijayakumar, K., Mayuram, M.,** and **Krishnamurthy, R.** Investigations into erosion wear performance of functionally graded chromium oxide–alumina titania ceramic composite deposits. *Mater. Sci. Forum*, 2003, **437–438**, 189–192.

21 **Hejwowski, T.** Wear resistance of graded coatings. *Vacuum*, 2002, **65**, 515–520.

22 **Prchlik, L., Sampath, S., Gutleber, J., Bancke, G.,** and **Ruff, A.** Friction and wear properties WC–Co and Mo–Mo_2C based functionally graded materials. *Wear*, 2001, **249**, 1103–1115.

23 **Yarrapareddy, E.** and **Kovacevic, R.** Unpublished work on the slurry erosion resistance of Ni–tung 60, A11-LVC tool steel and Inconel 625 laser based direct metal depositions, 2005.

24 **Westergard, R., Axen, N., Wiklund, U.,** and **Hogmark, S.** An evaluation of plasma sprayed ceramic coatings by erosion, abrasion and bend testing. *Wear*, 2000, **46**, 12–19.

25 **Khor, K.** and **Gu, Y.** Effects of residual stress on the performance of plasma sprayed functionally graded ZrO_2/NiCoCrAlY coatings. *Mater. Sci. Engng A*, 2000, **277**, 64–76.

26 See http://new.ametek.com/content-manager/files/par//powercorr.pdf

27 See http://www.cartech.com, *Ni-Tung Powders Technical Bull.*, 2004, 1–2.

28 **Hawthorne, H., Arsenault, B., Immarigeon, J., Legoux, J.,** and **Parameswaran, V.** Comparison of slurry and dry erosion behavior of some HVOF thermal sprayed coatings. *Wear*, 1999, **225–229**, 825–834.

29 **Finnie, I.** Some observations on the erosion of ductile materials. *Wear*, 1972, **19**, 81–90.

30 **Duan, C. G.** and **Karelin, V. Y.** Abrasive erosion and corrosion of hydraulic machinery, 2002, pp. 242–243 (Imperial College Press, London).

31 *ASTM metals test methods and analytical procedures*, ASTM Standard G 61–86 – Standard test method for conducting cyclic potentiodynamic polarization measurements for localized corrosion susceptibility of iron, nickel, or cobalt based alloys, 1999, Vol. 02–03, pp. 237–241 (American Society of Testing and Materials, Pennsylvania).

32 **Berget, J., Bardal, E.,** and **Rogne, T.** Influence of WC particle size and matrix composition on the behavior of WC–Co–Cr coatings sprayed by the HVOF process. In Proceedings of TMS United Thermal Spray Conference on *Thermal spray: a united forum for scientific and technological advances* (Ed. C. C. Berndt) 1997, pp. 783–789.